Polarization double-enhancement strategy to achieve super low energy consumption with ultra-high energy storage capacity in BCZT-based relaxor ferroelectrics

Zixiong Sun[a,b,c,d], Yuhan Bai[a], Hongmei Jing[e*], Tianyi Hu[f], Kang Du[g], Qing Guo[a], Pan Gao[a], Ye Tian[h], Chunrui Ma[f], Ming Liu[i*], Yongping Pu[h*]*

a School of Electronic Information and Artificial Intelligence, Shaanxi University of Science and Technology, Xi'an 710021, PR China

b Key Laboratory of Auxiliary Chemistry and Technology for Chemical Industry, Ministry of Education, Shaanxi University of Science and Technology, Xi'an 710021, PR China

c Shaanxi Collaborative Innovation Center of Industrial Auxiliary Chemistry and Technology, Shaanxi University of Science and Technology, Xi'an 710021, China

d MESA$^+$ Institute for Nanotechnology, University of Twente PO Box 217, 7522 NH Enschede, The Netherlands

e School of Physics and Information Technology, Shaanxi Normal University, Xi'an, 710119, PR China

f State Key Laboratory for Mechanical Behavior of Materials, Xi'an Jiaotong University, Xi'an, China.

g School of Mathematical and Physical Sciences, Wuhan Textile University, Wuhan, 430200, China

h School of Materials Science and Engineering, Shaanxi University of Science and Technology, Xi'an 710021, PR China

i School of Microelectronics, Xi'an Jiaotong University, Xi'an, China.

**Corresponding author: Zixiong Sun, Hongmei Jing, Yongping Pu*

E-mail address: SunZX@sust.edu.cn, jhmei.dengdai@snnu.edu.cn,

m.liu@xjtu.edu.cn puyongping@sust.edu.cn

Supplementary Information

1. Experimental procedure

1.1. Fabrication of (1-x)$Ba_{0.15}Ca_{0.85}Zr_{0.1}Ti_{0.9}O_3$-x$Bi(Zn_{2/3}Ta_{1/3})O_3$ ceramics

(1-*x*)$Ba_{0.15}Ca_{0.85}Zr_{0.1}Ti_{0.9}O_3$-*x*$Bi(Zn_{2/3}Ta_{1/3})O_3$ ceramics (*x*=0.02, 0.05, 0.10, 0.12, 0.15, 0.17, 0.20, 0.22) were prepared by a conventional solid-state reaction method. High-purity $BaCO_3$ (99%), $CaCO_3$(99%), TiO_2 (99.9%), ZrO_2 (99.8%), Bi_2O_3 (99%), ZnO(99%), Ta_2O_5(99%) powders were used as the raw materials. First, eight components of different proportions of $Ba_{0.15}Ca_{0.85}Zr_{0.1}Ti_{0.9}O_3$ and $Bi(Zn_{2/3}Ta_{1/3})O_3$ were weighed respectively according to the stoichiometric ratio. The raw materials were ball milled with deionized water as a medium using a planetary ball mill for 8 h at 300 rpm. After drying, each of the eight components was calcined at 1130°C-1150°C for 2 h. After grinding, they were again ball milled for 8 h and dried. Then the obtained powders were pressed into a disk with a diameter of 12 mm. Finally, the powders were maintained at a pressure of 200 MPa for 3 min through cold isostatic pressing. The pellets were sintered at 1150-1350℃ for 6h with a heating rate of 3℃ min^{-1} to obtain ceramic samples. What needs illustration is that we chose the conventional solid-state method because we would like to know the bottleneck of the energy storage performance of ceramic bulk prepared by such a low-cost technology. Compared to some other technologies, such as tape-casting and roll-forming, studying on solid-state method is of great significance to the preparation of pilot and even industrial-scale.

1.2. Characterization

The crystal structure of (1-*x*)$Ba_{0.15}Ca_{0.85}Zr_{0.1}Ti_{0.9}O_3$-*x*$Bi(Zn_{2/3}Ta_{1/3})O_3$ ceramics

was measured via X-ray diffraction (XRD D/max-2200PC, RIGAKU, Japan) with the step size of 0.01° and time per step of 0.05 s. The microstructures of the sintered ceramic samples were observed using scanning electron microscopy (SEM, Zeiss Sigma 300). The average grain size of the as-prepared specimens was counted by Nano Measurer Software with a statistical grain number of >100. The high-angle transmission electron microscope annular dark field (HR-TEM HAADF) measurements were performed by transmission electron microscopy (FEI Titan Cubed Themis G2 300). The dielectric properties(both ε-f and ε-T curves) and I-V characteristic measurement were measured using an impedance analyzer (E4980A, Agilent Technologies, USA) in the frequency range from 1 kHz to 1 MHz and the temperature range from −160 to 400 °C. To test the ferroelectric properties and pulse discharge behavior, the sintered ceramics were polished to a thickness of 100–180 μm, and then gold electrodes with a radius of 0.5 mm and 1.0 mm were sputtered on the surface, respectively. The corresponding P-E loops were obtained via a ferroelectric integrated test system (TF2000, aix ACCT, Germany), the discharge curves of $0.85Ba_{0.15}Ca_{0.85}Zr_{0.1}Ti_{0.9}O_3$-$0.15Bi(Zn_{2/3}Ta_{1/3})O_3$ ceramic were recorded using a charging-discharging measurement system (Tong guo (TG) technology, CFD-003, China). The X-ray photoelectron spectra (XPS, Thermo-Fisher ESCALAB 250Xi) were used to analyze the surface hydroxyls and the valence state of Ti and O elements. The absorption spectra were measured using a UV-vis spectrophotometer (PerkinElmer Lambda 35). Electron paramagnetic resonance (EPR) measurements were recorded by a Bruker EMX spectrometer (EMXnano, Bruker Instruments, Int.) at room temperature with microwave frequency (9.3 GHz).

1.3. The FORC distribution.

The FORC method is based on Preisach model and assumed the hysteresis loop consists of many minor loop (named as “hysterons”). In the FORC measurement, the electric field decreasing from positive saturation field E_{max} to E_r with an interval ΔE. We can caculate the “hysterons” distrbution through a set of FORC loops by follow formulas[1,2]:

$$\rho(E_r,E) = \frac{1}{2}\frac{\partial P^2(E_r,E)}{\partial E_r \partial E} \qquad \text{Eq. S1}$$

where $\rho(E_r,E)$ is the distribution density, E_r is the reversal electric field, E is the real electric field. In this work, we set E_{max} as 180 MV/cm and ΔE as 20 MV/cm, and measured 60 FORC loops for caculation.(Fig S4) We caculate the “hysterons” distribution and plot the contour plot as a function of E and E_r.

2. *Wei-bull* distribution

Before calculating the energy storage density(W_{rec}), the electric breakdown strength(E_b) of each film should be confirmed by employing the *Weibull* distribution, which can be expressed as follows:

$$X_i = \ln E_i \qquad \text{Eq. S2}$$

$$Y_i = \ln(- \ln(1 - P_i)) \qquad \text{Eq. S3}$$

$$P_i = \frac{i}{1 + n} \qquad \text{Eq. S4}$$

where X_i and Y_i are the two parameters of the Weibull distribution, Y_i varies linearly with X_i with a slope of β, E_i, and P_i are the sample's breakdown field and the electric field's failure probability distribution, respectively. While n, i, and β are the total number of specimens, the serial number of dielectric strength, and the slope of the linear relationship between $\ln(E_i)$ and $\ln(-\ln(1-P_i))$, respectively.

3. Calculation of *ESD* and η

The energy storage density(*ESD*) and η of a dielectric capacitor under a specific applied electrical field (*E*) can be represented by the following formula:

$$W_{\text{rec}} = \int_{P_m}^{P_r} E\mathrm{d}P \qquad \text{Eq. S5}$$

$$W_{\text{char}} = \int_{0}^{P_m} E\mathrm{d}P \qquad \text{Eq. S6}$$

$$\eta = W_{rec}/W_{sto}100\% \qquad \text{Eq. S7}$$

in which the W_{rec} and $W_{char,}$ are the *ESD* and energy-charged density(ECD) during one charge-discharge process, respectively. *P* is the generated polarization under *E*, and the P_m and P_r are the maximum polarization upon charging and the remanent polarization when the electrical field returns to zero, respectively.

4. Discussion of the contribution of the interfacial polarization

In general, dielectric materials, which are made up of atoms or molecules, possess four basic types of electric polarization: electronic polarization, ionic polarization, dipole/orientational polarization, and interfacial/space charge polarization. Each of them requires different times to switch and thus results in the decrease of dielectric constant with increasing electric field frequency. The total polarization of one dielectric material can be written as:

$$P = (\varepsilon_r - 1)\varepsilon_0 E = N\alpha E \quad \text{Eq. S8}$$

in which E is the applied external electric field on the dielectric material, and P is the total polarization triggered by E. The ε_r and ε_0 are the material's dielectric constants (or relative permittivity) and the vacuum permittivity, which equals $8.854*10^{-12}$ F/m, respectively. N is the number of induced dipole moments in unit volume, and the α is the polarizability of the dielectric.

When under static *DC* fields (applied electric frequency f=0), the contribution to P in Eq. S8 involves all the types of electric polarization mentioned above. The polarization contributed by the electronic polarization, ionic polarization, and orientational polarization can be written as:

$$P' = (\varepsilon_{r\infty} + \varepsilon_{ro} - 1)\varepsilon_0 E = N(\alpha_\infty + \alpha_o)E \quad \text{Eq. S9}$$

in which the $\varepsilon_{r\infty}$ and ε_{ro} are the dielectric constant when $f \rightarrow \infty$ and the dielectric constant contributed by the orientational polarization, respectively. Thus, the interfacial polarization (*Pi*) of a dielectric material should be:

$$P_i = P - P' = (\varepsilon_r - \varepsilon_{r\infty} - \varepsilon_{ro} - 1)\varepsilon_0 E = N(\alpha - \alpha_\infty - \alpha_o)E \quad \text{Eq. S10}$$

and the corresponding polarizability for the interfacial polarization should be :

$$\alpha_i = \alpha - \alpha_\infty - \alpha_o = (\varepsilon_r - \varepsilon_{r\infty} - \varepsilon_{ro})\varepsilon_0/N \quad \text{Eq. S11}$$

In this work, the interfacial polarization in the BCZT-*x*BZT ceramics should come from the interfacial area between the *C*-phase and *T*-phase(also the *PNR*s in higher BZT content ceramics), and it is valid to consider such an area as a whole. With increasing *x*, the latter's content decreases, indicating the decrement of the interfacial area, that is the *N* in Eq. S9, resulting in the decrement of interfacial polarization with increasing BZT content. In fact, not only the interfacial polarization but also some newly-formed dipole polarization (P_{dn}), which resulted from the lattice interdiffusion, exist in the interfacial area. According to the definition of dipole moment (p), which is expressed below:

$$p = \varepsilon_0 \alpha E_{local} = ql \quad \text{Eq. S12}$$

in which the E_{local}, q, and l are the electrical field applied on each unit cell, charge of the dipole and the distance between the center of the positive charge and the center of the negative charge in the dipole, respectively. Combined with Eq. S8 and Eq. S11, we can have the following formula below:

$$P_{dn} = \frac{3\varepsilon_r}{\frac{3\varepsilon_0}{N^2 ql} + \frac{2}{E}} \quad \text{Eq. S13}$$

which also shows that the P_{dn} has a positive correlation with the *N*, and thus should decrease with increasing BZT content.

5. The complete form of the defect equations

The Eq. 3 to Eq. 12 can be written as Eq. S14 to Eq. S23 as follows:

$$2Bi_2O_3 \xrightarrow{4(Ba_{0.85}Ca_{0.15})O} 4Bi_{(Ba_{0.85}\dot{Ca}_{0.15})} + V_{Ti_{0.9}Zr_{0.1}}^{''''} + 6O_O \quad \text{Eq. S14}$$

$$2(Zn_{2/3}Ta_{1/3})_2O_3 \xrightarrow{2(Ti_{0.90}Zr_{0.10})O2} 2(Zn_{2/3}Ta_{1/3})_{(Ti_{0.90}\acute{Zr}_{0.10})} + V_O^{\cdot\cdot} + 6O_O \quad \text{Eq. S15}$$

$$2Bi_2O_3 \xrightarrow{4(Ba_{0.85}Ca_{0.15})O} 4Bi_{(Ba_{0.85}\dot{Ca}_{0.15})} + V_{Ti_{0.9}Zr_{0.1}}^{''''} + 6O_O \quad \text{Eq. S16}$$

$$2(Zn_{2/3}Ta_{1/3})_2O_3 \xrightarrow{2(Ti_{0.90}Zr_{0.10})O2} 2(Zn_{2/3}Ta_{1/3})_{(Ti_{0.90}\acute{Zr}_{0.10})} + V_O^{\cdot\cdot} + 6O_O \quad \text{Eq. S17}$$

$$ZnO \xrightarrow{(Ba_{0.85}Ca_{0.15})O} Zn_{(Ba_{0.85}Ca_{0.15})} + O_O \quad \text{Eq. S18}$$

$$2Ta_2O_5 \xrightarrow{5(Ti_{0.90}Zr_{0.10})O2} 4Ta_{(Ti_{0.90}\dot{Zr}_{0.10})} + 4e' + 10O_O \quad \text{Eq. S19}$$

$$Ti^{4+} + e' \rightarrow Ti^{3+} \quad \text{Eq. S20}$$

$$2Bi_2O_3 \xrightarrow{4(Ba_{0.85}Ca_{0.15})O} 4Bi_{(Ba_{0.85}\dot{Ca}_{0.15})} + V_{Ti_{0.9}Zr_{0.1}}^{''''} + 6O_O \quad \text{Eq. S21}$$

$$4(Zn_{2/3}Ta_{1/3})_2O_3 \xrightarrow{4(Ba_{0.85}Ca_{0.15})O} 4(Zn_{2/3}Ta_{1/3})_{(Ba_{0.85}\dot{Ca}_{0.15})} + V_{Ti_{0.9}Zr_{0.1}}^{''''} + 12O_O \quad \text{Eq. S22}$$

$$2(Zn_{2/3}Ta_{1/3})_2O_3 \xrightarrow{2(Ti_{0.90}Zr_{0.10})O2} 2(Zn_{2/3}Ta_{1/3})_{(Ti_{0.90}\acute{Zr}_{0.10})} + V_O^{\cdot\cdot} + 6O_O \quad \text{Eq. S23}$$

6. The physical meaning of the abbreviations in the band diagram analyzing

E_{VAC}: the vacuum level

E_{FA}: the Fermi energy level of the Au electrode

$E_{F\text{-}B}$: the Fermi energy level of the BCZT-BZT ceramic

$E_{C\text{-}B}$: the conduction band of the BCZT-BZT ceramic

$E_{V\text{-}B}$: the valence band of the BCZT-BZT ceramic

ϕ_A: the work function of the Au electrode

ϕ_B: the work function of the BCZT-BZT ceramic

χ_B: the electron affinity of the BCZT-BZT ceramic

ϕ_s: the Schottky barrier height

ϕ_b: the build-in potential

V: the external applied voltage

R_d: the depletion region

L_I: the equivalent layer of insulator

L_C: the equivalent layer of conductor

7. Explanation of the *Schottky* barrier formation

Fig. S10(a) shows the band diagram of the Au/BCZT-0.15BZT interface before contact. As the Au work function is higher than the electron affinity of ceramic,[3,4] once connected, the Fermi level of both Au and BCZT-0.15BZT should be aligned, which leads to band bending in the interface. According to the defect reaction Eq. 5-9, the majority of carriers in BCZT-0.15BZT are electrons. Thus, it can be regarded as *n*-type semiconductors under the linear electric field range in Fig. 5(b2).[5] The electrons would drift from the ceramic side to the Au side and a depletion layer(R_d) with the direction pointing to Au formed in the interface formed, as displayed in Fig. S10 (b). More electrons will be trapped in R_d and finally, a build-in potential(Φ_b) formed. When applying a forward external voltage(V) pointing from ceramic to electrode, as seen in Fig. S10 (c), the BCZT-0.15BZT Fermi level moves down, increasing the Φ_b to Φ_b+V and R_d to R_d'. In this case, more electrons were trapped in the interface, and the current spread was blocked.

8. Finite Element Simulation

The *COMSOLMultiphysics6.0* linking with *Matlab5.2* was employed to simulate the potential and electric field distribution and the current spread. The *Voronoi* diagram in *Matlab5.2* was chosen to describe the geometry of the BCZT-*x*BZT ceramics, and each polygon was identified as one ferroelectric domain. Compared to the *T*-phase in the BCZT-0.02BZT, the *T*-phase in the BCZT-0.15BZT was set to have a smaller domain size and quantity to fit the microstructure characterization.

Once the breakdown happens, the film will undergo an irreversible transformation, widely believed to be the joint effect of electric and thermal fields. Based on this, the *AC/DC module* and *heat transfer module* in *COMSOLMultiphysics6.0* are both called, and the physical model can be expressed as follows:

The electrical breakdown process was described according to the spread of current density with the boundary conditions meeting:

$$\boldsymbol{n}\cdot\boldsymbol{i}=0 \qquad \text{Eq. S24}$$

where $\boldsymbol{n}$ and $\boldsymbol{i}$ are the normal vector and current density vector, respectively. This boundary condition means that no electric current flows into the boundary. The constitutive relations

$$\boldsymbol{J}=\sigma\boldsymbol{E} \qquad \text{Eq. S25}$$

$$\boldsymbol{J}=A^{*}T^{2}\exp\left[\frac{-q(\phi_S-\sqrt{q\boldsymbol{E}/4\pi\varepsilon_r\varepsilon_0})}{kT}\right] \qquad \text{Eq. S26}$$

which is the standard Ohmic's contact and Schottky contact, respectively, and

$$\boldsymbol{D}=\varepsilon_0\varepsilon_r\boldsymbol{E} \qquad \text{Eq. S27}$$

where $\boldsymbol{J}$ and $\boldsymbol{E}$ are the current density and external electrical field, respectively, and σ and ε_r are

each material's electrical conductivity and dielectric constant (permittivity), which needs input in the model. ε_0 is vacuum permittivity with a value of 8.854187817*10^{-12} F/m. The A^*, k, q, ε_0, and ε_r, which won't change with external factors, are the effective Richardson constant, Boltzmann's constant, electronic charge, vacuum dielectric constant, and relative dielectric constant, respectively.[6] In this work, the Ohmic's contact was applied in the BCZT-xBZT ceramics with x=0.02 and 0.22(Eq. S24), and the Schottky contact was applied in that with x=0.15(Eq. S26), and the Schottky barrier height was used as 1.4 eV.[7] The dielectric constant of the *T*-phase, which is marked with the *T* in each domain is filled with ~10000 and the *C*-phase, which is the rest part of each ceramic, has a dielectric constant of ~7000.

Considering the stationary equation of continuity of the model after a long time, Eq. S25 and 26 should be changed to a more general form:

$$\boldsymbol{J}=\sigma\boldsymbol{E}+\frac{\partial \boldsymbol{D}}{\partial t}+\boldsymbol{J_e} \qquad \text{Eq. S28}$$

$$\boldsymbol{J}=A^*T^2\exp\left[\frac{-q(\emptyset_S-\sqrt{q\boldsymbol{E}/4\pi\varepsilon_r\varepsilon_0})}{kT}\right]+\frac{\partial \boldsymbol{D}}{\partial t}+\boldsymbol{J_e} \qquad \text{Eq. S29}$$

At the same time, current conservation should be met from then on with the equations:

$$\nabla\cdot\boldsymbol{J}=Q_{j.v} \qquad \text{Eq. S30}$$

$$\boldsymbol{E}=-\nabla V \qquad \text{Eq. S31}$$

where $Q_{j.v}$ and $\boldsymbol{D}$ represent the change rate of electric charge per unit volume and the electric displacement vector. $\boldsymbol{J_e}$ is the current density and density of the external electric current, and V denotes the electrical potential. Here, we use the *If sentence*, which is written as *if(ht. alpha>0.1,6e6,0.04)* and was input in the software to determine if a breakdown occurred or not.

It means if the breakdown happens, the σ takes the 6e6; otherwise, it takes 0.04. The *ht. alpha* is the physical name of $\frac{\partial \alpha}{\partial t}$, which represents an anisotropic thermal diffusivity(α).

The heat transfer in solid interface solves for the following equation derived from:

$$d_z(\rho C_p)_{eff}\frac{\partial T}{\partial t} + d_z(\rho C_p)_{\text{eff}}\boldsymbol{u}\cdot\nabla T + \nabla\cdot\boldsymbol{q} = d_z Q + q_0 + d_z Q_{ted} \quad \text{Eq. S32}$$

in which the $\boldsymbol{u}$ is the fluid velocity vector, and the $\boldsymbol{q}$ is the conductive heat flux that is written as:

$$\boldsymbol{q} = -d_z k_{eff}\nabla T \quad \text{Eq. S33}$$

and the d_z, $k_{eff,}$ and ∇T are the thickness of the domain in the out-of-plane direction, effective thermal conductivity, and temperature perturbation, respectively. The $(\rho Cp)_{eff}$ is the effective volumetric heat capacity at constant pressure that is composed of two parts:

$$(\rho C_p)_{eff} = \theta_{it}k_{it} + (1 - \theta_{it})k \quad \text{Eq. S34}$$

where the θ_{it} and k are the fraction of transformation and thermal conductivity, respectively, and the θ_{it} can be expressed as:

$$\theta it = \min(\alpha_b, 1) \quad \text{Eq. S35}$$

where the α_b is the fraction of film that was broken down to correspond to the whole film. The Q in Eq. S32 is the heat source and is defined as:

$$Q = -\rho L_{it,h}\frac{\partial \theta_{it}}{\partial t}(T > T_{it.h}) \quad \text{Eq. S36}$$

where the T_{it}, t_{it}, and L_{it} are the transformation temperature, transformation time, and the enthalpy change when the electric breakdown happens.

The following formula should be satisfied when the *heat transfer module* is coupled with the *AC/DC module*.

$$\frac{\partial \alpha}{\partial t} = \frac{1}{t_{it,h}} (T > T_{it,h})$$ Eq. S37

Once the electric breakdown happens, the $\frac{\partial \alpha}{\partial t}$ changes, so the σ mentioned above also changes. In our work, the T_{it} and t_{it} are set to be 150 ^{o}C and 0.01ns, respectively, according to the literatur.[8-10] The serial number of the *COMSOLMultiphysics6.0* and *Matlab5.2* is offered by the University of Twente.

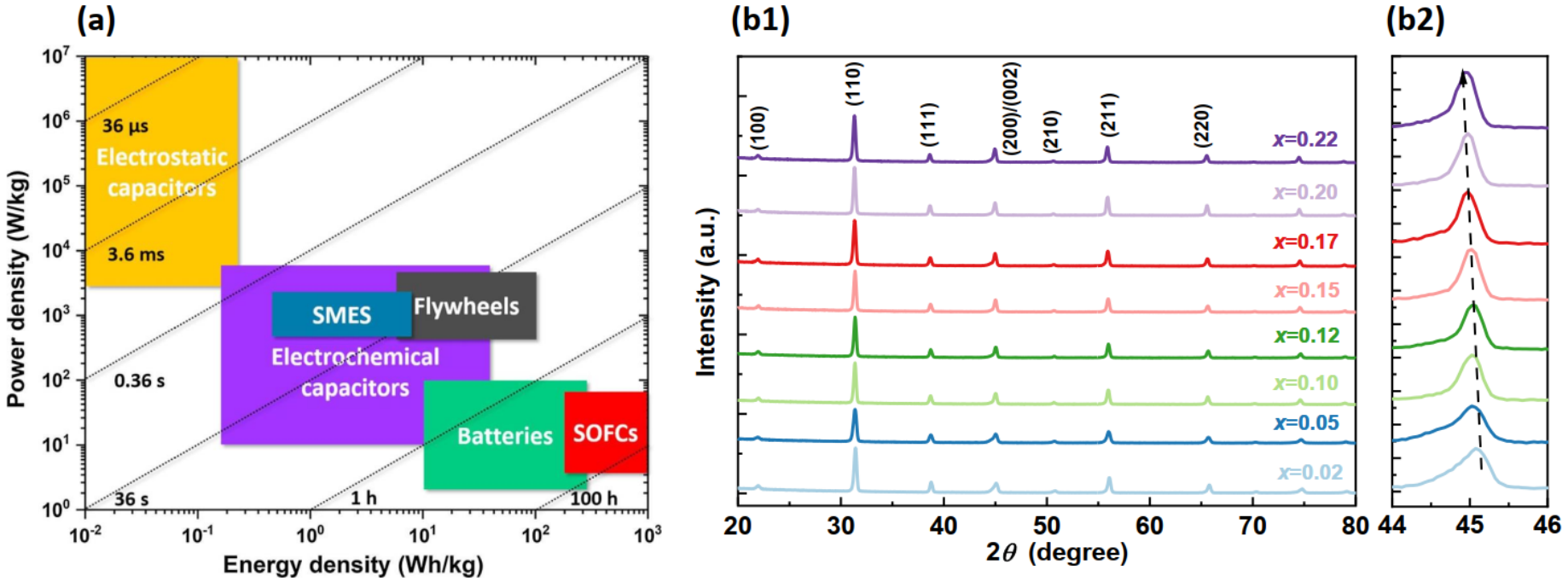

Fig. S1 (a) Ragone plot of the four different energy storage devices from some representative literature. Reproduced with permission.7 Copyright 2018, Elsevier[11]; (b1) XRD scan from 2θ=20 °~80 ° of BCZT-xBZT with x=0.02-0.22; (b2) enlarged-view from 2θ=44 °~46 ° of (b1) .

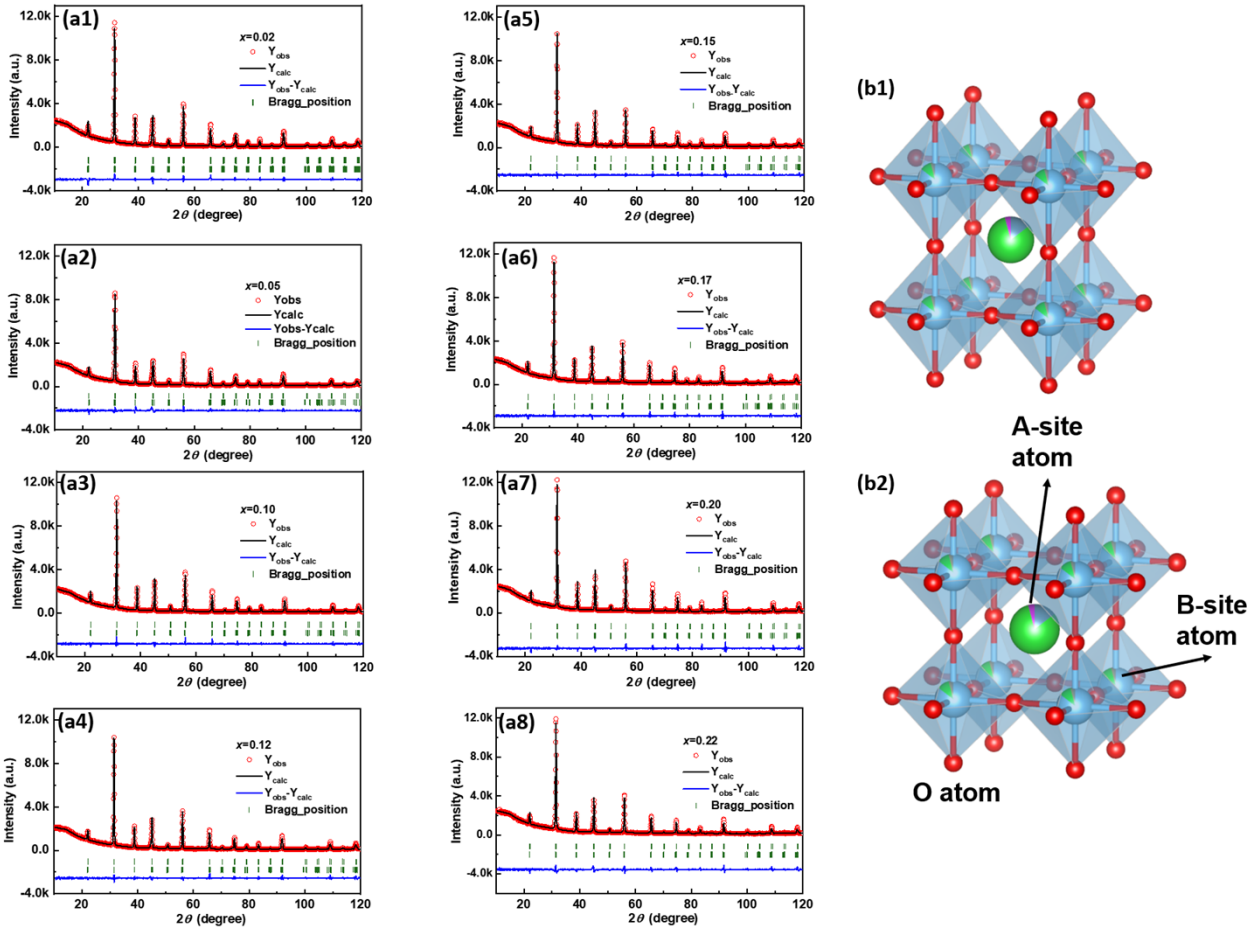

Fig. S2 (a1)-(a8) Rietveld XRD refinement of BCZT-xBZT with x=0.02-0.22; ball- stick model of the (b1) T-phase(p4mm); (b2) C-phase(pm3m) in this work, and each atom is marked.

Tab. S1 Parameters of the Rietveld XRD refinement result and the phase content of BCZT-xBZT with x=0.02-0.22.

x	R_p	R_{wp}	Chi^2	***T-Phase content* (%)**	***C-Phase content* (%)**
0.02	5.20	7.90	3.14	31.8	68.2
0.05	5.10	7.98	2.92	24.6	75.4
0.10	5.05	7.68	2.68	17.1	82.9
0.12	4.83	7.61	2.63	14.6	85.4
0.15	4.70	7.48	2.62	11.6	88.4
0.17	5.08	8.18	3.40	9.8	90.2
0.20	5.68	9.39	4.46	8.4	91.6
0.22	6.01	9.9	5.56	8.1	91.9

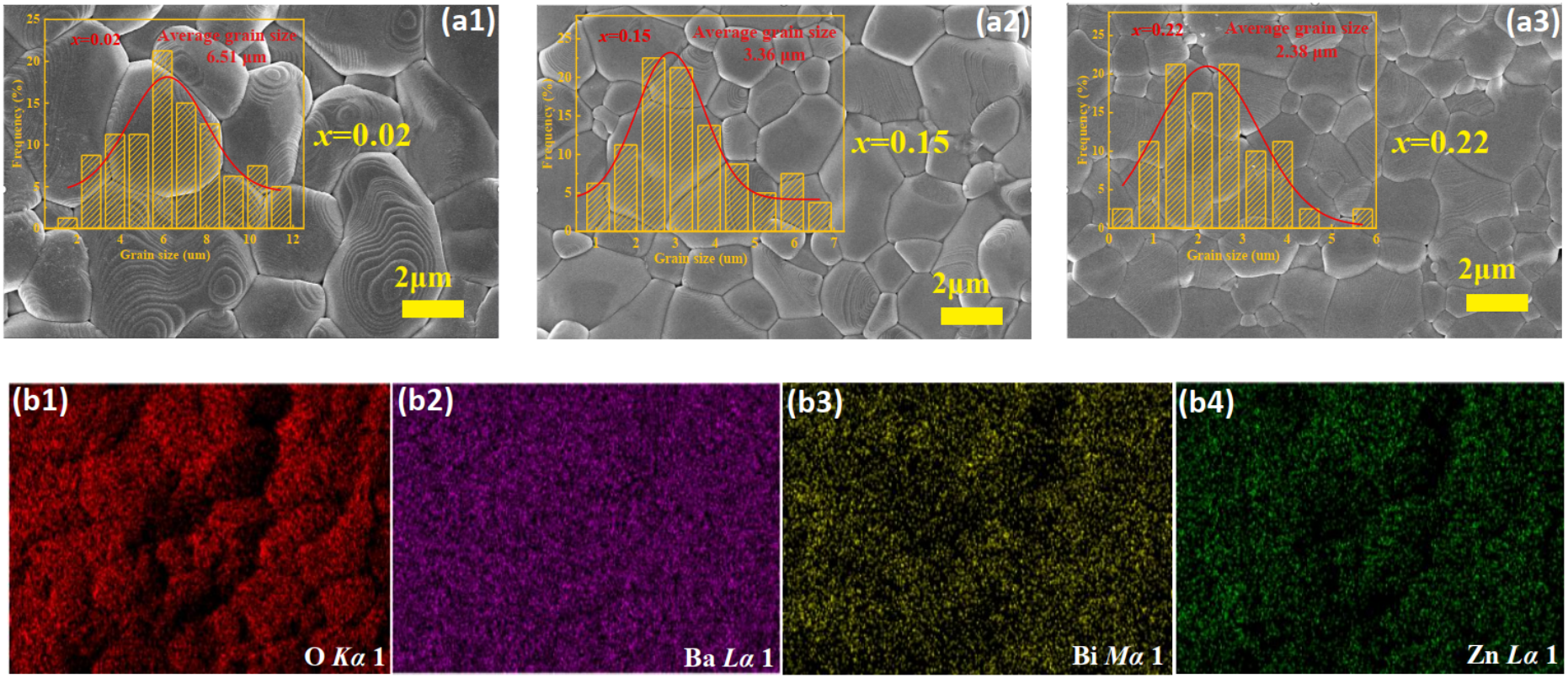

Fig. S3 (a1)-(a3) SEM image of BCZT-xBZT with x=0.02, 0.15, and 0.22; (b1)-(b4) EDS mapping for Kα 1, Ba Lα 1, Bi Mα 1, and Zn Lα 1 of BCZT-0.15BZT.

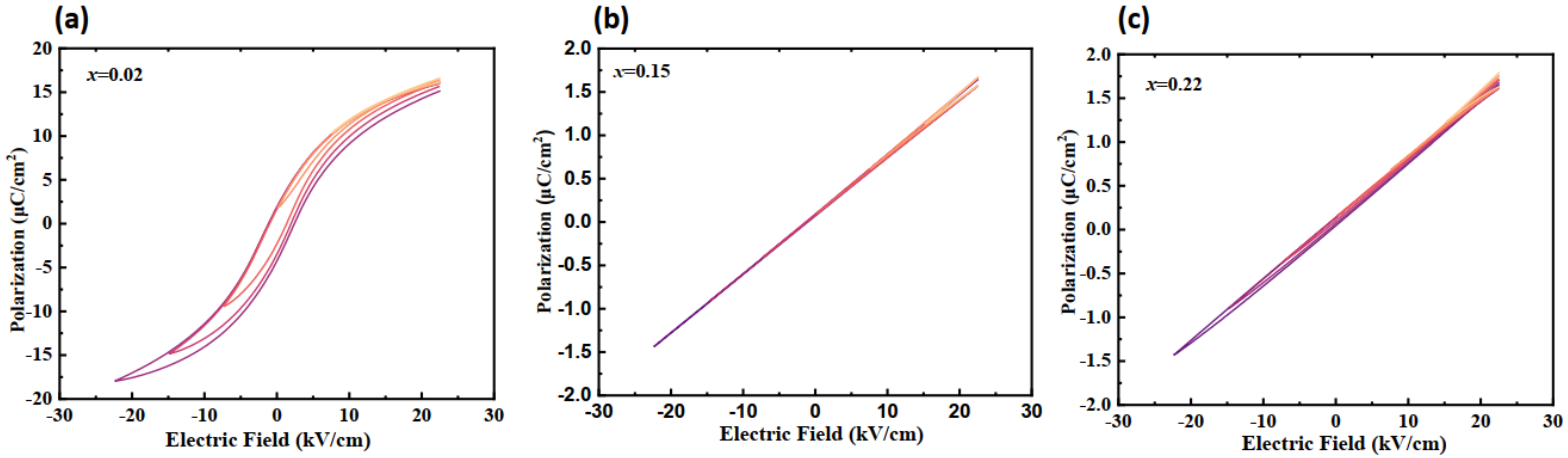

Fig. S4 (a)-(c) the FORC loop of BCZT-xBZT with x=0.02, 0.15, and 0.22.

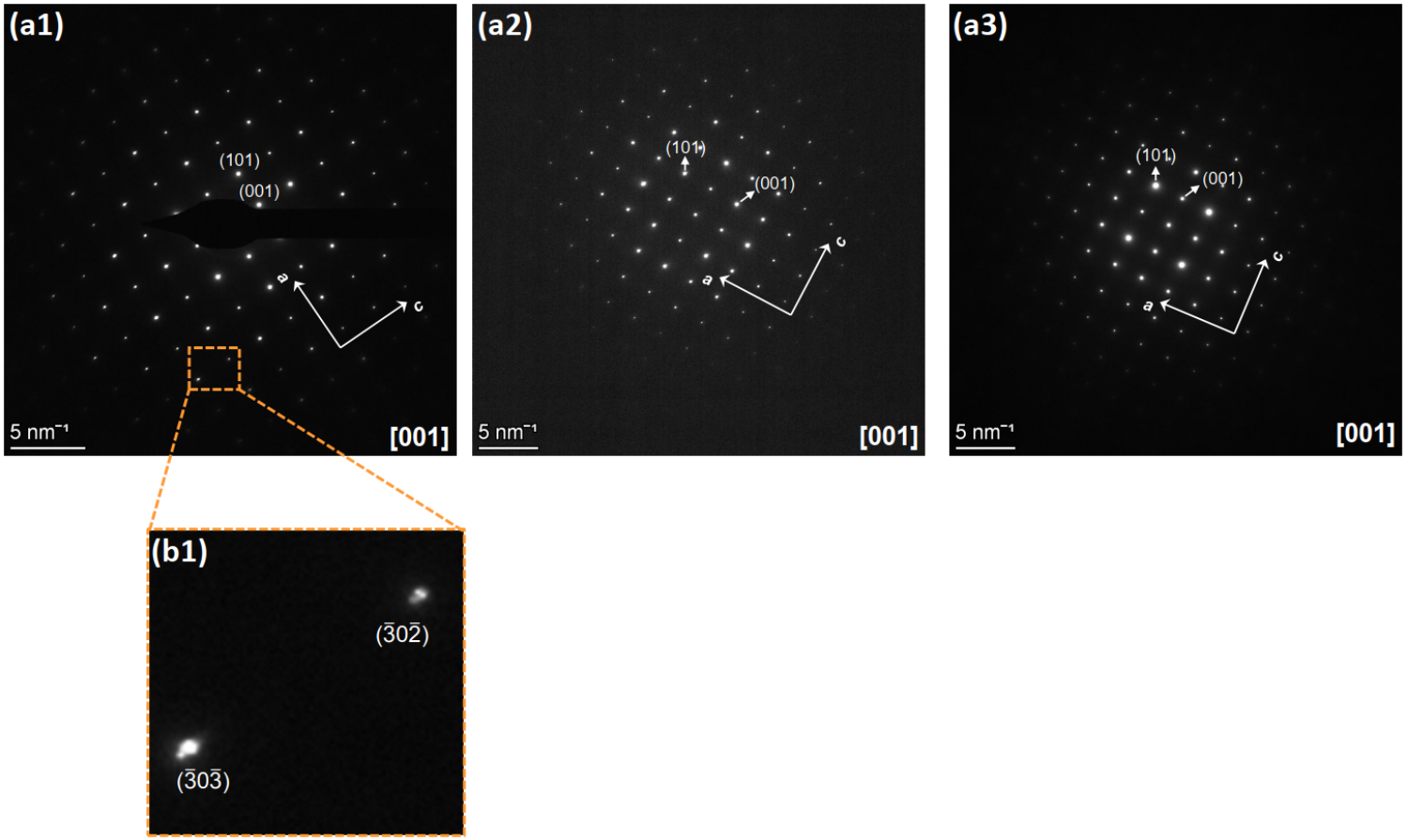

Fig. S5 (a1)-(a3) SAED patterns taken from the transparent red area in Fig. 1(c1)-(c3); (b) Enlarged view of the dashed rectangle circled area in Fig. S4 (a1).

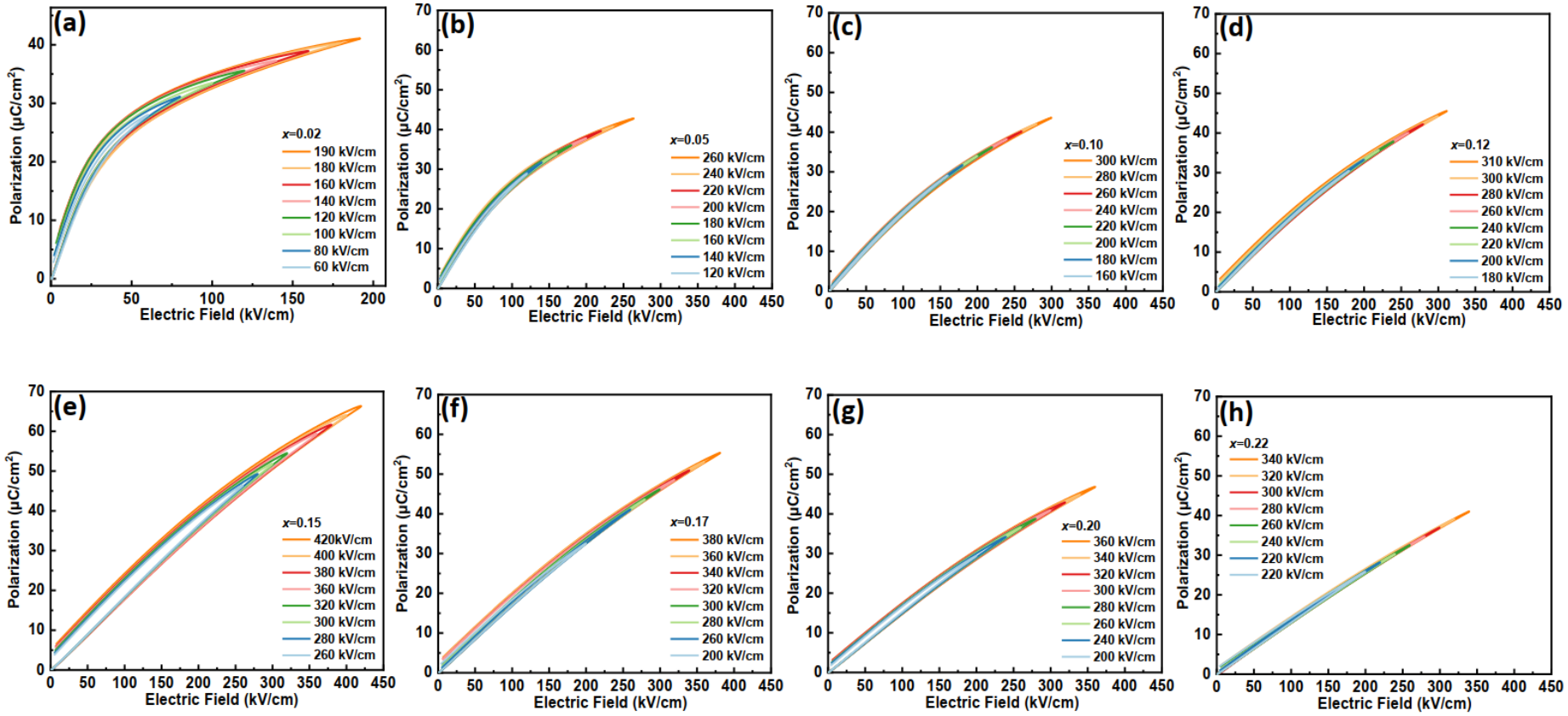

Fig. S6(a)-(h) unipolar *P-E loops of BCZT-xBZT with x=0.02-0.22 at different electric fields.*

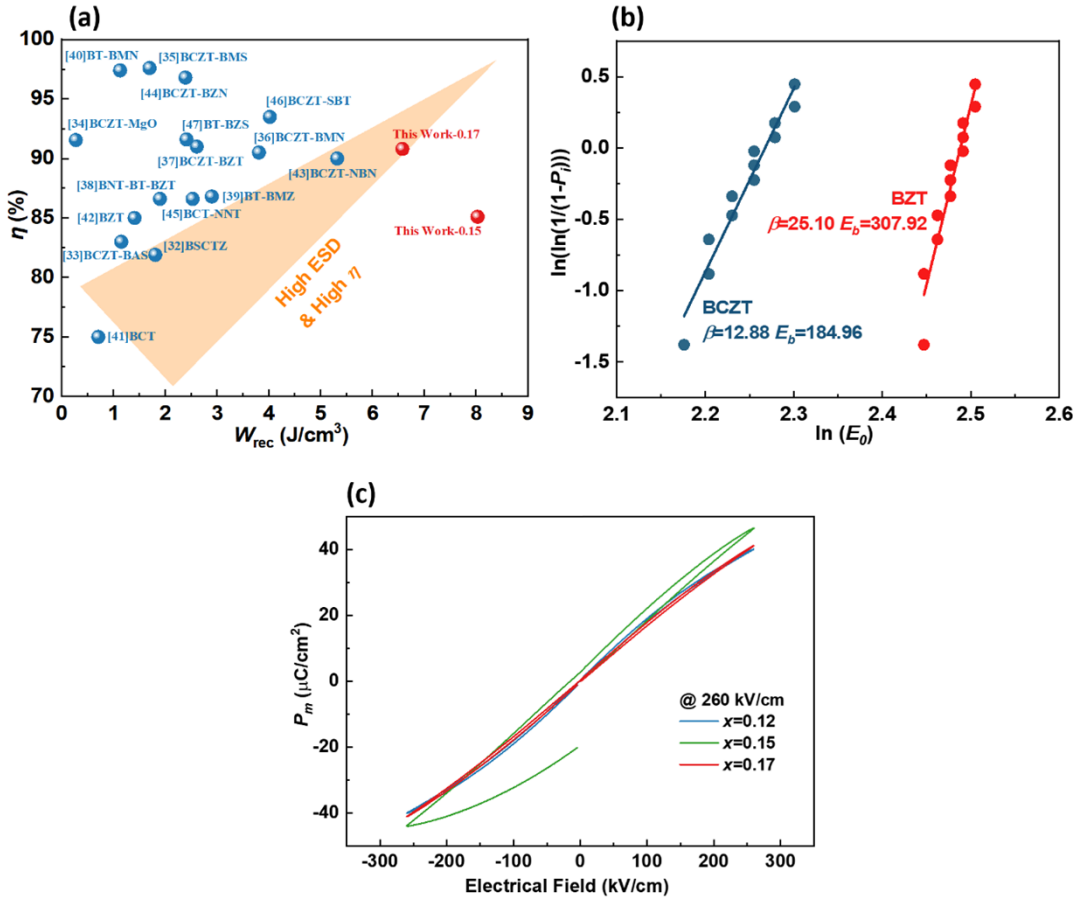

Fig. S7 (a) Comparison of the W_{rec} and η between BCZT-xBZT with x=0.15 and 0.17 in our work and some typical BZT-based ceramics (The references marked in Fig. (a) are based on the References part in the main manuscript); (b) Wei-bull distribution of pristine BCZT and BZT; (c) bipolar P-E loops of BCZT-xBZT with x=0.12, 0.15, and 0.17 under 260 kV/cm.

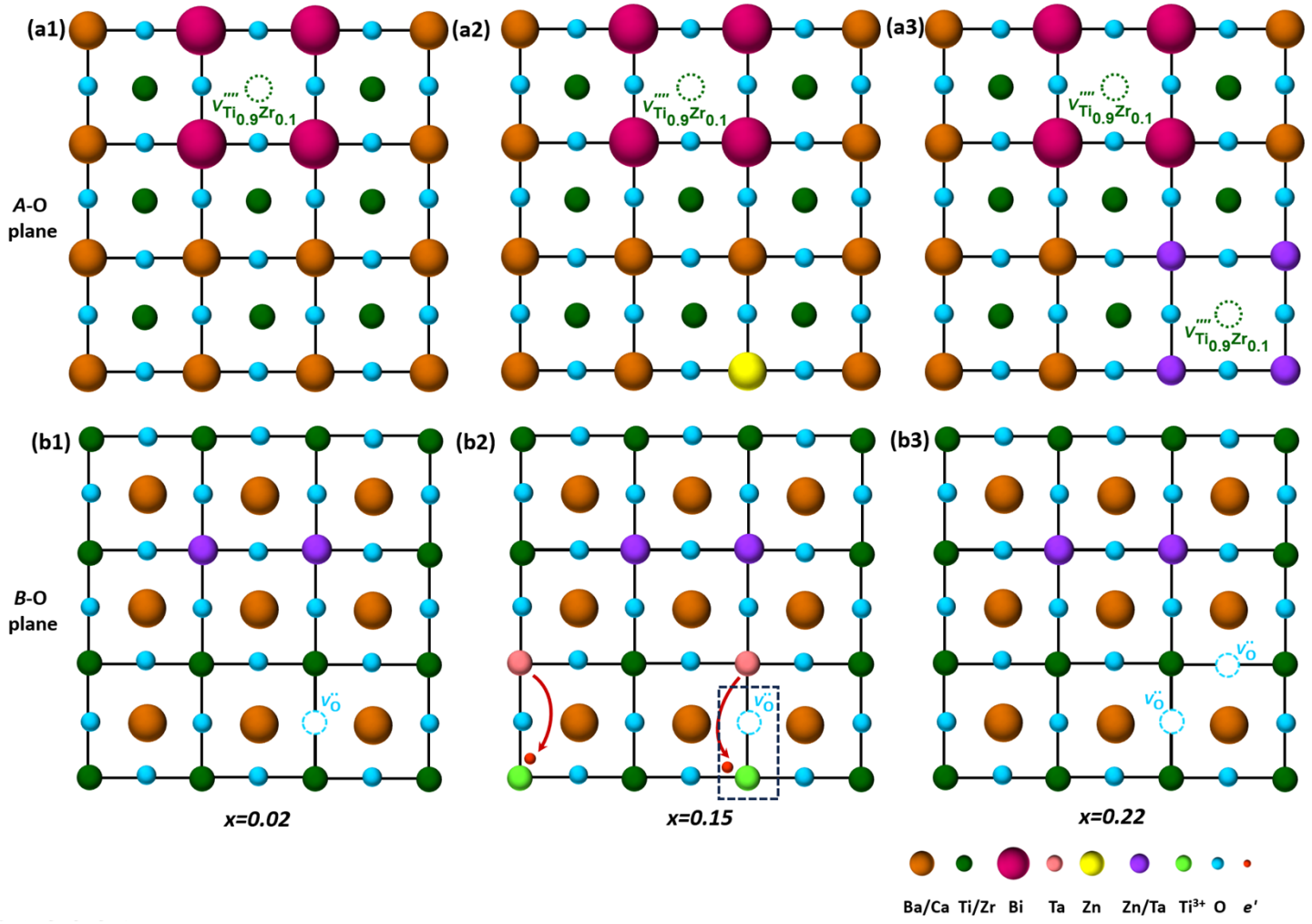

Fig. S8 sketch of the lattice of (a1)-(a3) A-O plane; (b1)-(b3) B-O plane to explain the defect equations of BCZT-xBZT with x=0.02, 0.15, and 0.22.

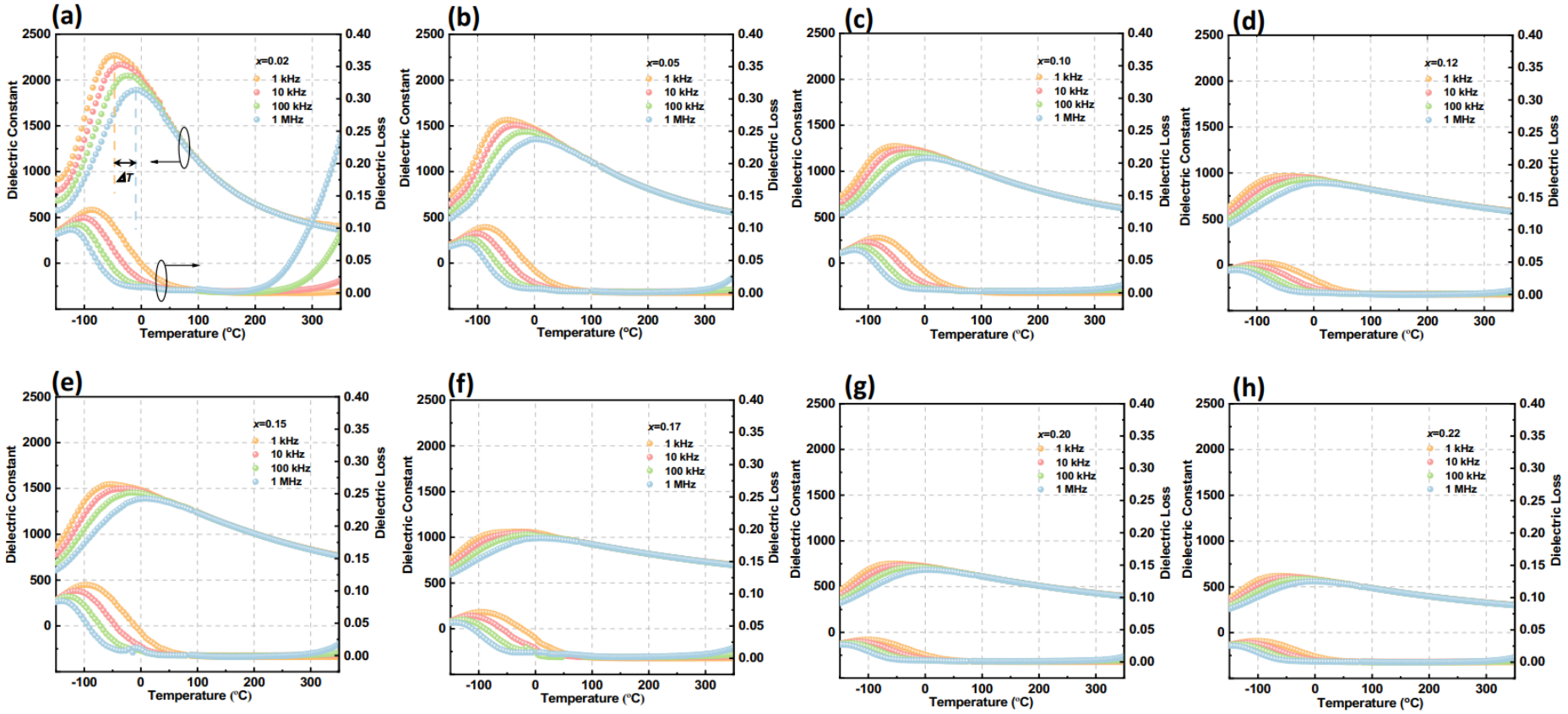

Fig. S9 the ε-T curves and tan δ-T curves of BCZT-xBZT with x=0.02-0.22.

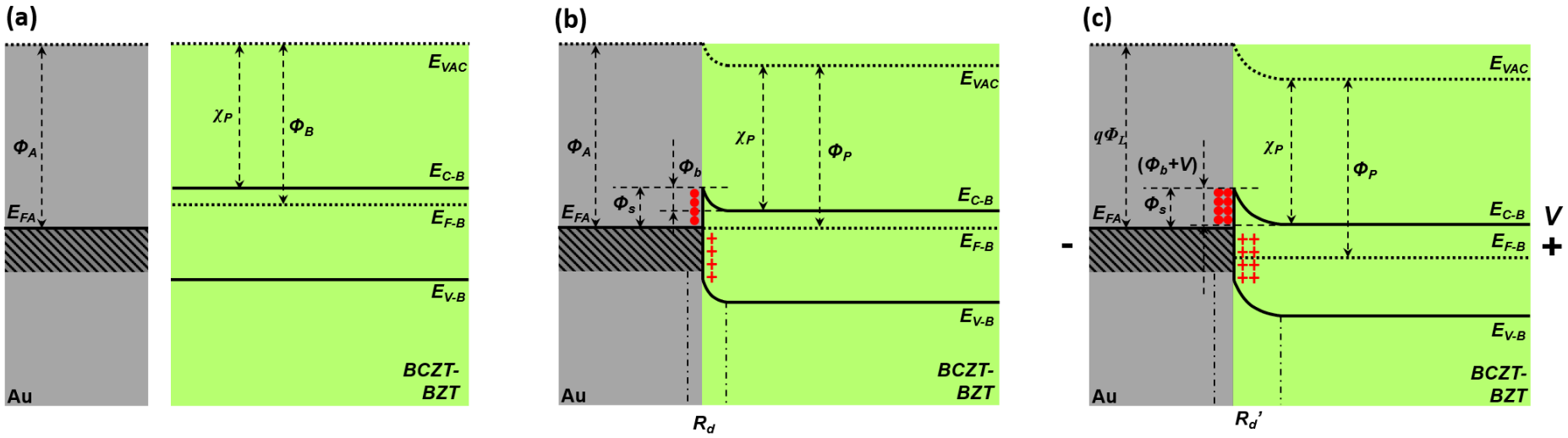

Fig. S10 the band diagram of the interface between Au electrodes and BCZT-0.15BZT (a) before contact; (b) after contact; (c) under V.

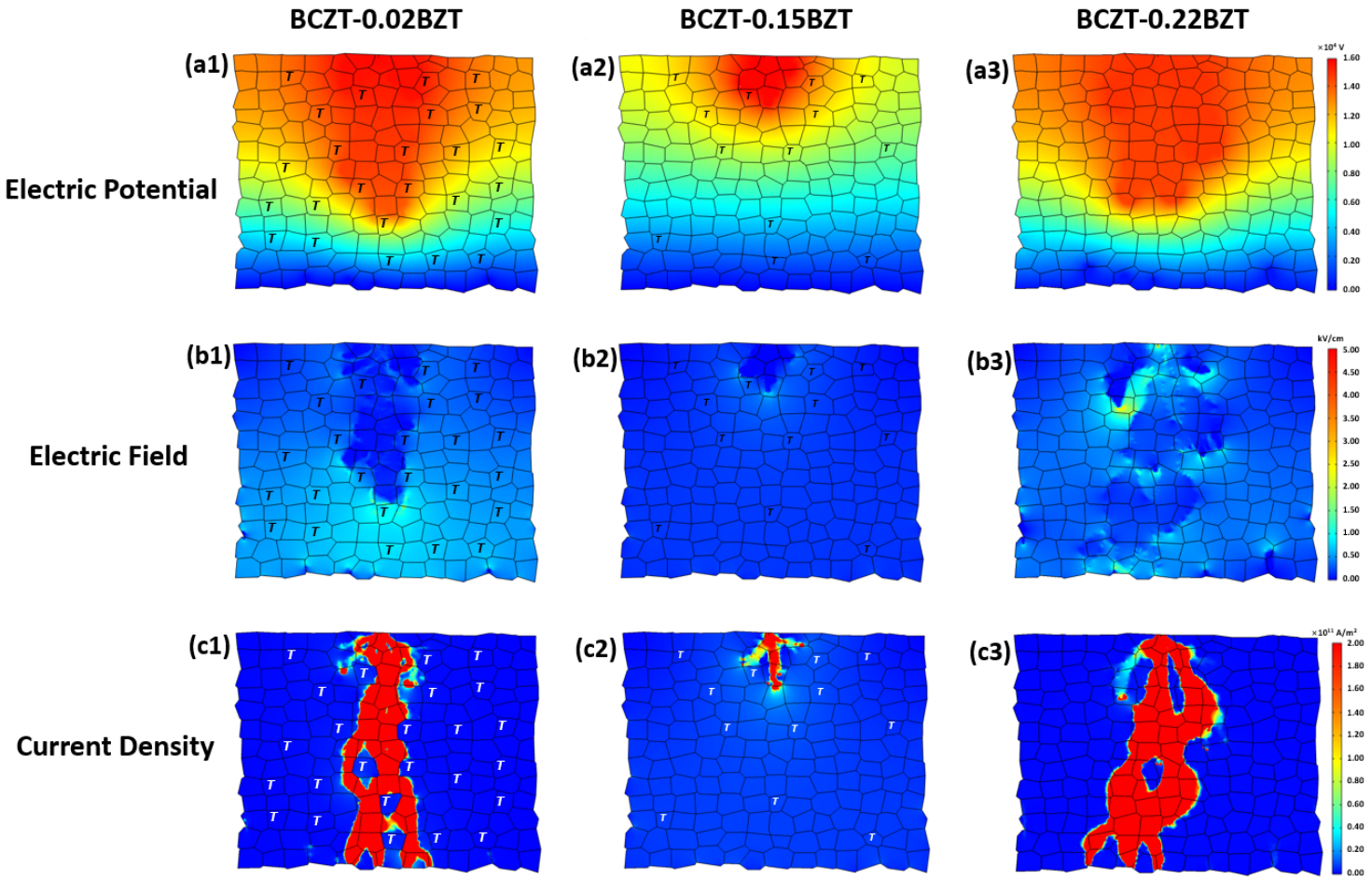

Fig. S11 (a1–a3) Electric potential distribution; (b1–b3) the electric field distribution; (c1–c3) The spread of the current density of BCZT-xBZT with x=0.02, 015 and 0.22.

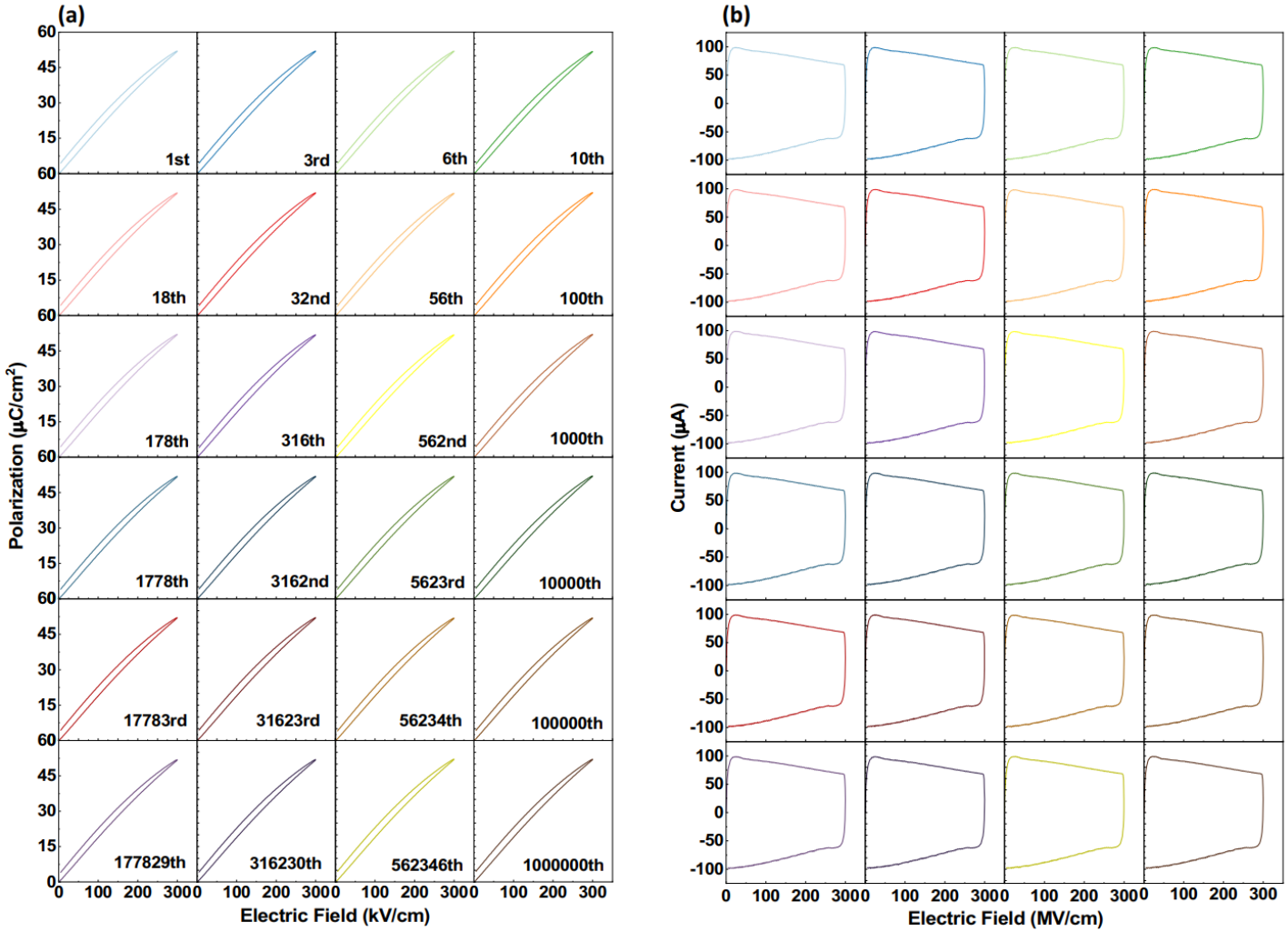

Fig. S12 (a) unipolar *P-E* loops*; (b)* unipolar *I-E curves of BCZT-0.15BZT at different cycle numbers from 1st to 106th at room temperature of BCZT-0.15BZT.*

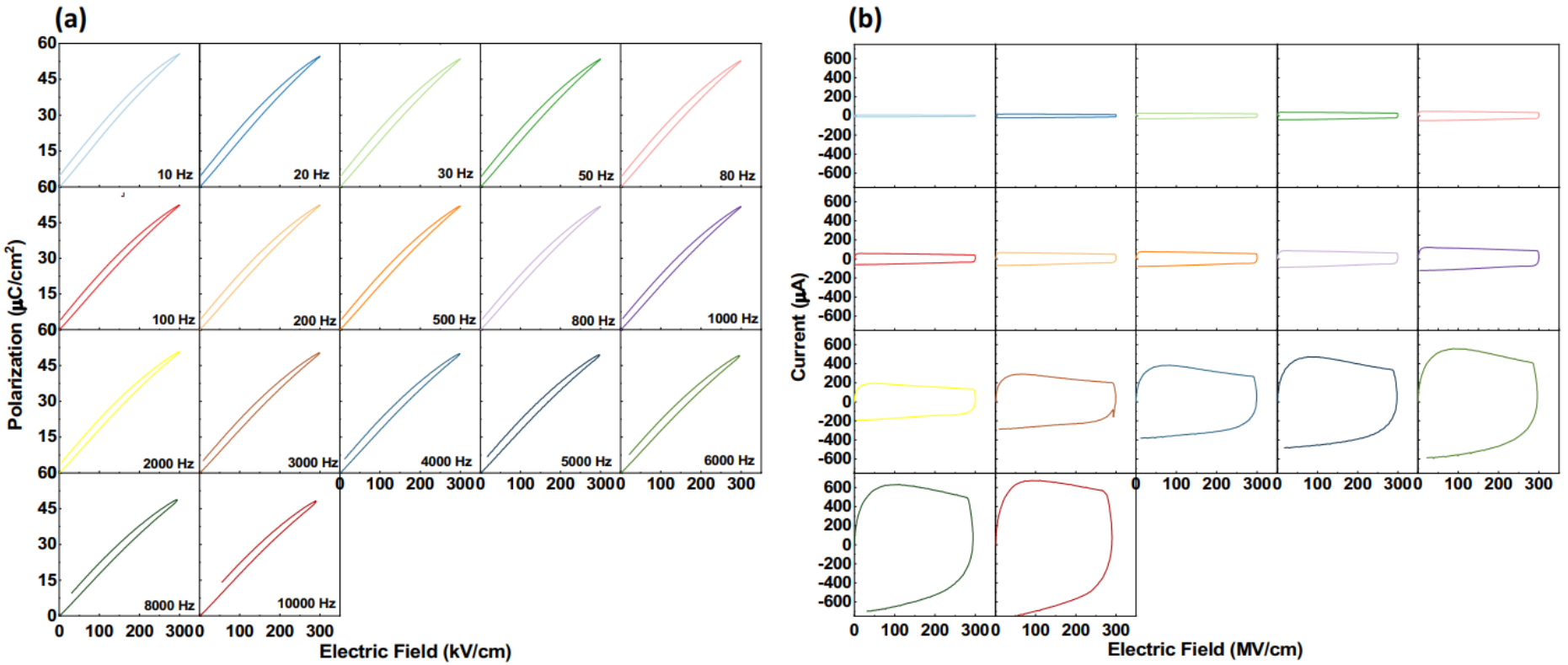

Fig. S13 (a) unipolar *P-E loops; (b)* unipolar *I-E curves of BCZT-0.15BZT at different frequencies from 10 Hz to 10000 Hz at room temperature of BCZT-0.15BZT.*

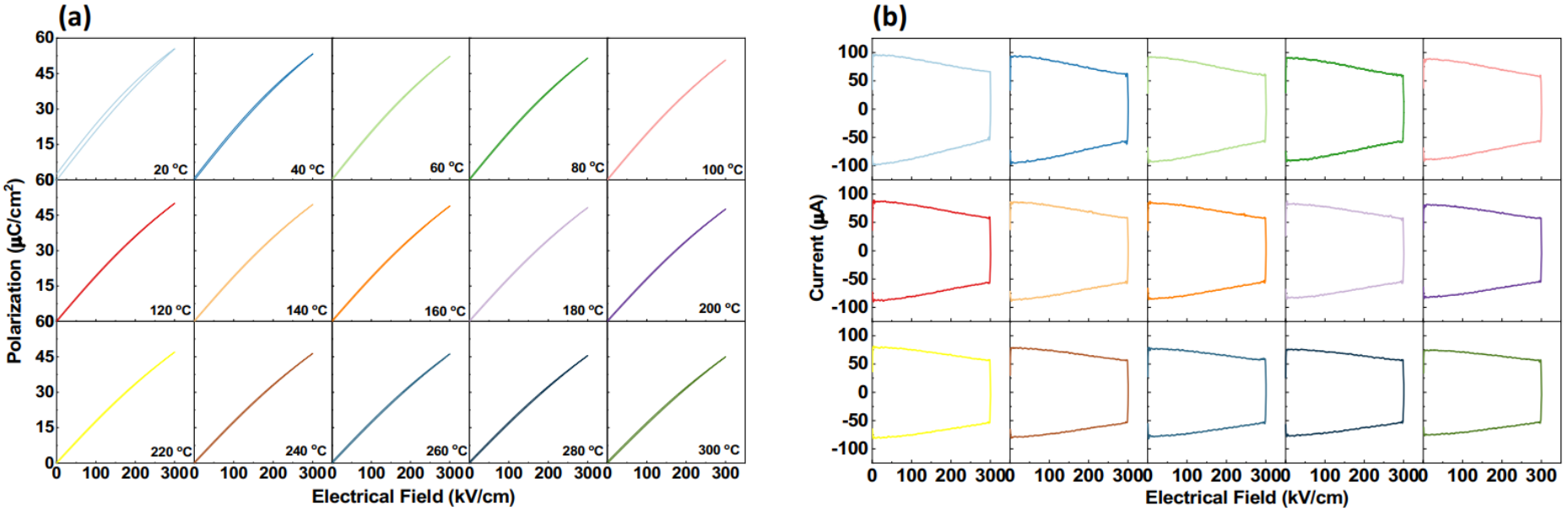

Fig. S14 (a) unipolar *P-E loops; (b)* unipolar *I-E curves of BCZT-0.15BZT at different temperatures from 25 °C to 300 °C of BCZT-0.15BZT.*

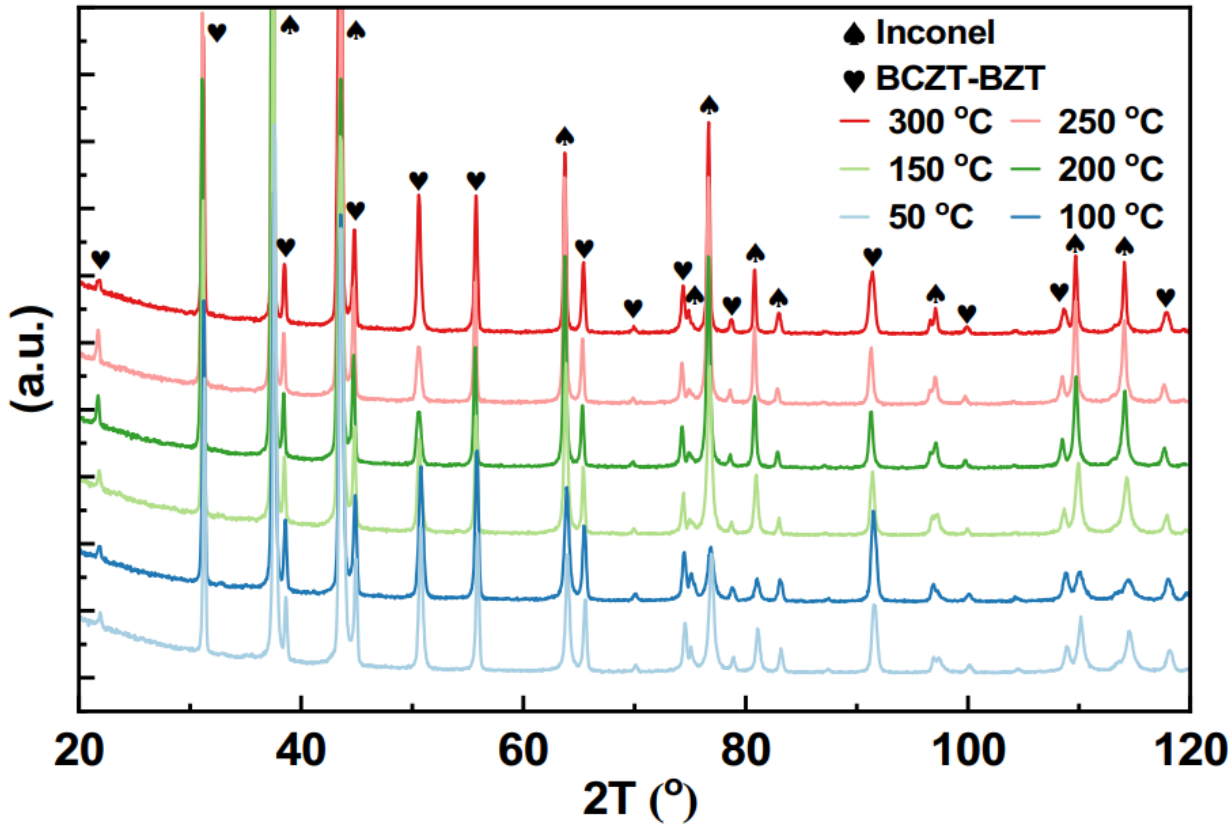

Fig. S15 HT-XRD scans of BCZT-0.15BZT from 20° to 120° at the temperature range from 50 °C to 300 °C.

Tab. S2 Parameters of the metal cation in BCZT-xBZT ceramic

Parameter	A-site			B-site			
Atom	Ba	Ca	Bi	Zr	Ti	Zn	Ta
Valence	+2	+2	+3	+4	+4	+2	+5
Coordination	12	12	12	6	6	6	6
Inoic Radius (Å)	1.61	1.34	1.31	0.72	0.605	0.74	0.64

References

[1] T. Hu, C. Ma, Y. Dai, Q. Fan, M. Liu, C. Jia, Enhanced Energy Storage Performance of Lead-Free Capacitors in an Ultrawide Temperature Range via Engineering Paraferroelectric and Relaxor Ferroelectric Multilayer Films, *ACS Appl. Mater. Inter.* 2020, 25930-25937.

[2] C. Wang, X. Yang, Z. Wang, C. He, X. Long, Investigation of switching behavior of acceptor-doped ferroelectric ceramics, *Acta Mater.* 2019, **170**, 100-108

[3] Z. Sun, S. Huang, W. Zhu, Y. A. Birkhölzer, X. Gao, R. A. Avila, H. Huang, X. Lou, E. P. Houwman, M. D. Nguyen, G. Koster, G. Rijnders, *APL Materials* 2023, **11**, 101129.

[4] Z. Sun, J. Liu, H. Wei, Q. Guo, Y. Bai, S. Zhao, S. Wang, L. Li, Y. Zhang, Y. Tian, X. Zhang, H. Jing, Y. Pu, S. Zhang, *J. Mater. Chem. A* 2023, **11**, 20089–20101.

[5] J. Dong, J. Han, Y. Liu, A. Nakajima, S. Matsushita, S. Wei, W. Gao, *ACS Appl. Mater. Interfaces* 2014, **6,** 1385–1388.

[6] F.-C. Chiu, *Advances in Materials Science and Engineering*, 2014, **2014**, 578168.

[7] K. N. S. Schuldt, H. Ding, J. C. Jard, J. Koruza, A. Klein, Phys. *Status Solidi A*, 2021, **218**, 2100143

[8] M. Hikita, M. Nagao, G. Sawa and M. Ieda, *Journal of Physics D: Applied Physics*, 1980, **13**, 661.

[9] N. Meng, X. Ren, G. Santagiuliana, L. Ventura, H. Zhang, J. Wu, H. Yan, M. J Reece and E. Bilotti, *Nature communications*, 2019, **10**, 4535.

[10] J. Huang, Y. Zhou, Z. Zhou and R. Liu, *AIP Advances*, 2016, **6**, 095026.

[11] L. T. Yang, X. Kong, F. Li, H. Hao, Z. X. Cheng, H. X. Liu, J. F. Li, S. J. Zhang, *Prog. Mater. Sci.* 2019, **102**, 72.